Earth and Planetary Science Letters 296 (2010) 255–266

Contents lists available at ScienceDirect

Earth and Planetary Science Letters

journal homepage: www.elsevier.com/locate/epsl

Reconciling Pacific 410 and 660 km discontinuity topography, transition zone shear velocity patterns, and mantle phase transitions

Christine Houser *, Quentin Williams

Department of Earth and Planetary Sciences, University of California Santa Cruz, 1156 High Street, Santa Cruz, CA, 95064, USA

ARTICLE INFO

Article history:
Received 29 June 2009
Received in revised form 30 April 2010
Accepted 12 May 2010
Available online 22 June 2010

Editor: L. Stixrude

Keywords:
660 km discontinuity
transition zone
phase transformations

ABSTRACT

We observe that the depths of the 410 and 660 km seismic discontinuities are, on average, slightly positively correlated globally. This is due in large part to a modestly depressed 660 km discontinuity and a large depression of the 410 km discontinuity across the Pacific. The Clapeyron slope (dP/dT), the change in pressure (depth) of a phase transition with a change in temperature, can be used to predict the depth of a phase transformation assuming lateral temperature variations. The phase change of olivine to β-spinel is well understood experimentally, almost certainly produces the 410 km discontinuity, and has a positive Clapeyron slope. At the base of the transition zone, both the olivine component of the mantle (γ-spinel) and the pyroxene component (garnet) transform to perovskite and periclase. Observations of 660 km discontinuity depths are often consistent with the negative Clapeyron slope of the γ-spinel to perovskite and periclase transition, with an apparent anti-correlation with the depth of the 410 km discontinuity. However, under the Pacific, the depression of the 410 km discontinuity and slow seismic velocities indicate that the mantle is warmer than average. Using a negative Clapeyron slope for the perovskite-forming reaction, the 660 km discontinuity is predicted to be shallow in this region. However, we observe that it is either depressed or has little deflection from its average depth. We find that if the Clapeyron slope associated with the 660 km discontinuity changes sign from negative to positive between 1920 and 2020 K, we can explain the correlation of discontinuity structure with seismic velocities in the transition zone. This shift in sign is in accord with the dominant 660 km transition-forming reaction shifting from γ-spinel to garnet near this temperature.

1. Introduction

Since the first comprehensive studies of the 1D structure of the Earth (Jeffreys and Bullen, 1940), it has been observed that there are rapid increases in seismic velocities in the depth range between 400 and 700 km depth. By the 1960s, predictions from mineral physics based on analog compounds placed phase changes in the olivine component of the mantle within this depth range (Anderson, 1967). The possibility that the mantle might undergo layered convection often involved a connection between these seismic discontinuities and a possible chemical boundary layer. However, the agreement between mineral physics experiments and the global mapping of the seismic discontinuities at approximately 410 km and 660 km depth has led to the acceptance of these features as due predominantly to the phase transformations from olivine to β-spinel, and γ-spinel to perovskite and periclase, respectively. Hence, considerable effort has been devoted to determining accurate values of the Clapeyron slopes of these transitions (Stixrude, 1997; Ito and Katsura, 1989; Fei et al., 2004; Katsura et al., 2004; Akaogi et al., 2007). The Clapeyron slope, the change in pressure with change in temperature (dP/dT), of a phase transformation as well as the influences of chemistry and mineralogy on these transitions have been examined (Ita and Stixrude, 1992; Weidner and Wang, 2000; Hirose, 2002). Meanwhile, seismic studies have concentrated on determining the variations in the depths of the 410 and 660 km discontinuities on local and global scales as well as other features such as the width of, and velocity contrast across the transitions (e.g., (Shearer, 2000; Lawrence and Shearer, 2006a)). Combining the results of mineral physics and seismology allows us the prospect of not only constraining the absolute temperature and bulk chemistry of the transition zone, but also their lateral variations.

One useful technique for determining the depth of the 410 and 660 km discontinuities is analysis of upgoing *P* waves that are converted to *S* waves at the boundary, which are known as *PdS* phases (*d* refers to the conversion depth). The time lapse between the initial *P* arrival and the converted *S* arrival is used to determine the discontinuity depth assuming a 1D velocity model. This technique, known as "receiver function" analysis (Langston, 1979), deconvolves the vertical component *P* phase from the radial component *SV* phase to enhance and normalize the signal of the converted phase before stacking (Vinnik, 1977). Receiver functions can provide detailed mapping of discontinuity

* Corresponding author.
E-mail address: cthouser@ucsc.edu (C. Houser).

0012-821X/$ – see front matter © 2010 Elsevier B.V. All rights reserved.
doi:10.1016/j.epsl.2010.05.006

depths in localized regions on scales of hundreds of kilometers, but only in the vicinity of multi-component seismic stations. Some receiver function studies combine results for many stations to find the average transition zone thickness for large regions (Bostock, 1996; Vinnik et al., 1996; Ramesh et al., 2002; Lebedev et al., 2003) or for the globe (Chevrot et al., 1999; Lawrence and Shearer, 2006b). Other such studies concentrate on specific tectonic environments and often map topography as a function of azimuth around a station. Studies beneath hot spots in the Pacific (Shen et al., 1998; Owens et al., 2000; Li et al., 2000a; Li et al., 2003; Hooft et al., 2003) generally have found that the transition zone thins beneath these regions. However, subduction zone studies (Li et al., 2000b; Collier et al., 2001; Lebedev et al., 2002; Saita et al., 2002; Ai et al., 2003; van der Meijde et al., 2005; Ramesh et al., 2005; Tonegawa et al., 2005) find that the transition zone thickens in these cold regions. For comprehensive reviews of transition zone structure see Helffrich (2000) and Shearer (2000).

Global mapping of topography of the 410 and 660 km discontinuities became possible in the early 1990s due to the expansion of the global seismic network. Revenaugh and Jordan (1991) used *ScS* reverberations while Shearer (1991) used stacks of long-period records to determine topography on the 410 and 660 km discontinuities. Both studies found peak-to-peak topography on the discontinuities to be no more than 25 km for long wavelengths. This low amplitude topography provided definitive evidence that the transition zone discontinuities are not due to a chemical boundary, which would have larger topography in response to dynamic deformation from convective upwellings and downwellings, including subduction.

Here, we use underside reflections off the 410 and 660 km discontinuities which arrive as precursors to *SS*, the surface reflection of the *S* phase (Fig. 1). Initial *SS* precursor studies found ~30 km peak-to-peak topography on the 410 and 660 km discontinuities (Shearer and Masters, 1992; Shearer, 1993). These analyses were later expanded upon with more data for *SS* precursors (Flanagan and Shearer, 1998) and *PP* precursors (Flanagan and Shearer, 1999). Gu et al. (1998) and Gu et al. (2003) also mapped global 410 and 660 km discontinuity topography with *SS* precursors using a different methodology than that of Flanagan and Shearer (1998). However, both groups' maps of 410 and 660 km discontinuity topography and hence transition zone thickness are highly correlated. Recently, Chambers et al. (2005) used *P410P* and *S410S* to produce individual and joint maps of global 410 km discontinuity topography with features that differ from the previous *SS* precursor studies. Houser et al. (2008a), using *SS* precursors, found the 410 and 660 km discontinuities are uncorrelated or only slightly correlated at global scales. This result was also noted by Gu et al. (1998), and requires an explanation since *SS* precursors are the main type of data providing global coverage of both discontinuities. However, *SS* precursors can resolve only the long wavelength features (thousands of kilometers) of the discontinuities due to the broad extent of the Fresnel zone at their bounce point. Lawrence and Shearer (2008) use a more rigorous mapping of *SS* precursor times to their Fresnel zone pattern by implementing finite frequency kernels, and still find similar patterns of topography of the discontinuities as the previous ray-theory-based studies.

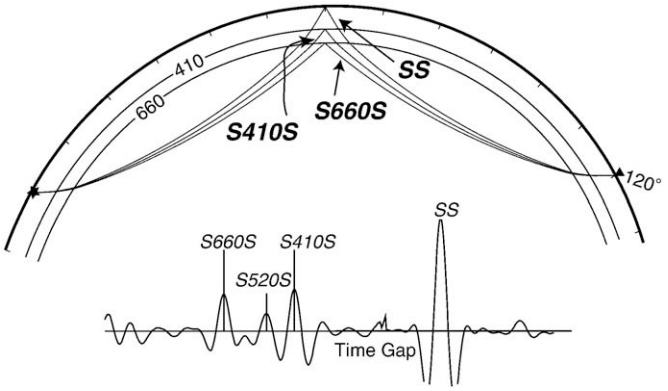

Fig. 1. Top: ray geometry of *SS* precursors. Bottom: actual precursor stack used in this study from the NW Pacific including 445 seismograms. There is a time gap between the main *SS* arrival and the precursors.

The importance of the observed correlation of 410 and 660 km discontinuity topography is that they are generally expected to be anti-correlated based on most mineral physics studies. The phase transformation of olivine to β spinel is well known to have a positive Clapeyron slope (dP/dT), such that higher temperatures will move the phase transformation to higher pressures (i.e. greater depth) (e.g., (Akaogi et al., 2007)). Likewise, colder temperatures will move the phase transformation to lower pressures (i.e. shallower depths). This relationship is reversed for the 660 km discontinuity as the phase transformation of γ-spinel to perovskite and periclase is known to have a negative Clapeyron slope (Akaogi et al., 2007). Therefore, a coherent, $(Mg,Fe)_2SiO_4$ dominated, and through-going thermal anomaly is expected to produce anti-correlated topography of the 410 and 660 km discontinuities. As described above, most studies of topography in regions with thermal anomalies (hot spots and subduction zones) do show the expected anti-correlated discontinuity topography. Despite the chemical heterogeneity in these regions, especially in subduction zones, the discontinuities appear to be dominantly influenced by the thermal structure coupled with the phase diagram of olivine. Hence, we have a conundrum: how does the long wavelength structure of the mantle lead to correlated or non-correlated 410 and 660 km discontinuity topographies when mantle structural variations are likely dominantly thermal?

To answer this question, we first examine the geographic patterns of the discontinuities to reveal where they are the most correlated and anti-correlated. Then, we examine the relationship of the discontinuity topography to the shear velocity structure in the transition zone. We find that the main deviation from the predicted anti-correlated topography occurs under the Pacific plate where there is a depression of the 410 km discontinuity along with low shear wave speeds. Thus, under the Pacific, an associated rise in the 660 km discontinuity would be expected, but instead it is flat or depressed in this region. We combine this observation with mineral physics studies of the transition zone phases at high temperature to conclude that the warm transition zone under the Pacific causes an aluminous mantle assemblage to be dominated by majorite which then transforms to perovskite with a small positive Clapeyron slope (Hirose, 2002), and that the *SS* precursors predominantly reflect off of this majorite to perovskite transition. As a result, the 410 and 660 km discontinuities are anti-correlated in cold subduction zones and, on average, are slightly positively correlated in hot regions. Since the subduction zones are relatively narrow features relative to the broad warm regions, the positive correlation dominates at long wavelengths. Hence, the correlation of these discontinuities, absent major non-adiabatic vertical temperature perturbations between 410 and 660 km, may provide a constraint on the nature of the 660 km discontinuity at different regions of the planet.

2. Topography maps

We use the latest maps of discontinuity topography and transition zone thickness from Houser et al. (2008a) and briefly summarize their data and methods here. The data consist of *SS* phases that span from 1976 to 2005. The 1976–1995 data are those compiled by Flanagan and Shearer (2000) (13,500 traces) and the 1995–2005 data are those compiled by Houser et al. (2008b) (26,300 traces). Houser et al. (2008a) combined the *SS* phases from these two studies to assemble the largest compilation of *SS* phases to date. Since the shear impedance contrasts that define the 410 and 660 km discontinuities are around 4% and 8%, respectively, for PREM (Dziewonski and Anderson, 1981) or 6–12% and 7–13% (Shearer and Flanagan, 1999),

the reflected phases from these discontinuities tend to be small in amplitude. Thus, the traces must be aligned and stacked to amplify their signal above the noise level of most seismograms. The alignment and stacking procedure is described in Flanagan and Shearer (2000), and the modifications to their algorithm are given in Houser et al. (2008a). All the traces that fall in a circular 5° radius bin are aligned on the peak of the *SS* phase and then stacked, resulting in stacked traces with approximately 5° spacing for the entire globe and can be found on the corresponding author's website. However, bins with less than 6 traces per stack are not included in the mapping, and thus some regions, such as off the west coast of South America, are sparsely covered. The depths are determined by measuring the differential *SS-SdS* time where *SdS* is the *SS* phase that is reflected off of a discontinuity at depth, *d*. The times are converted to depths from predicted travel times for precursor arrivals using PREM (Dziewonski and Anderson, 1981) and have been corrected for the global crustal model CRUST 2.0 of Laske et al., (http://mahi.ucsd.edu/Gabi/rem.dir/crust/crust2.html). The 410 and 660 km discontinuity topography has also been corrected for velocity structure in the upper mantle and transition zone using shear tomographic model HMSL-S06 (Houser et al., 2008b).

The maps of 410 and 660 km discontinuity topography are provided in Fig. 2. Spherical splines are computed from the cap measurements and interpolated at regular intervals of 5° in longitude and latitude. The splines minimize the squared Laplacian integrated over the sphere and thus smooth out short wavelength (high harmonic degree) structure (Parker, 1994). Fitting our data to χ^2/N of 0.5 results in a model that is the equivalent of a spherical harmonic truncation at about degree twenty. The black line in the bottom graph of Fig. 2 shows the correlation of the 410 and 660 km discontinuity maps as a function of spherical harmonic degree. This approach reveals that the two discontinuities are non-correlated or slightly positively correlated on a global scale at long wavelengths. Since this study concentrates on observations under the Pacific plate, we also plot a theoretical correlation (grey line) for the case that the 660 km discontinuity topography is anti-correlated to that of the 410 km discontinuity under the Pacific plate. This theoretical case demonstrates that the pattern under the Pacific has a large effect on the low-order harmonics. Thus, if it is possible to bring the topography and shear velocity observations under the Pacific into accord with the current knowledge of phase changes in the transition zone, then we can reconcile the non-correlation seen at global scales with the anti-correlation observed at regional scales.

A number of regional studies do find that the discontinuities are anti-correlated in subduction zones, and this anti-correlation is also seen in the long wavelength topography along the western Pacific. The 410 km discontinuity is shallow and the 660 km discontinuity is depressed along a swath spanning from New Zealand up to Tonga–Fiji, across to Sumatra, and extending from southeast Asia up to the Aleutian Islands. The 660 km discontinuity is depressed underneath South America as well, but there is little topography on the 410 km discontinuity in this region. However, a detailed look at the northern part of South America using *SS* precursors shows that the 410 and 660 km discontinuities are mostly correlated except for across the northernmost tip of the continent (Schmerr and Garnero, 2007). One of the most striking features of the 660 km discontinuity is the extremely shallow region under eastern Africa which is accompanied by a slight rise in the 410 km discontinuity, resulting in a thin transition zone. Initial receiver function studies of this region showed an average transition zone thickness (Nyblade et al., 2000). However, more recent work using a larger dataset (Benoit et al., 2006) finds that the 410 km discontinuity reflection, while weak, appears to be slightly depressed with a large rise (~20 km) of the 660 km discontinuity which would indicate a thermal origin for the transition zone thinning. The 410 km and 660 km discontinuities are both shallow near Antarctica and under western North America. Surprisingly, the most prominent feature of the 410 km discontinuity topography, a large depression under most of the central and western Pacific plate, has no expression in the 660 km discontinuity topography. The Pacific plate encompasses a large portion of the Earth and this non-correlation beneath the Pacific plate is a major contributor to the global observation of non-correlated discontinuity topography at low harmonic degrees.

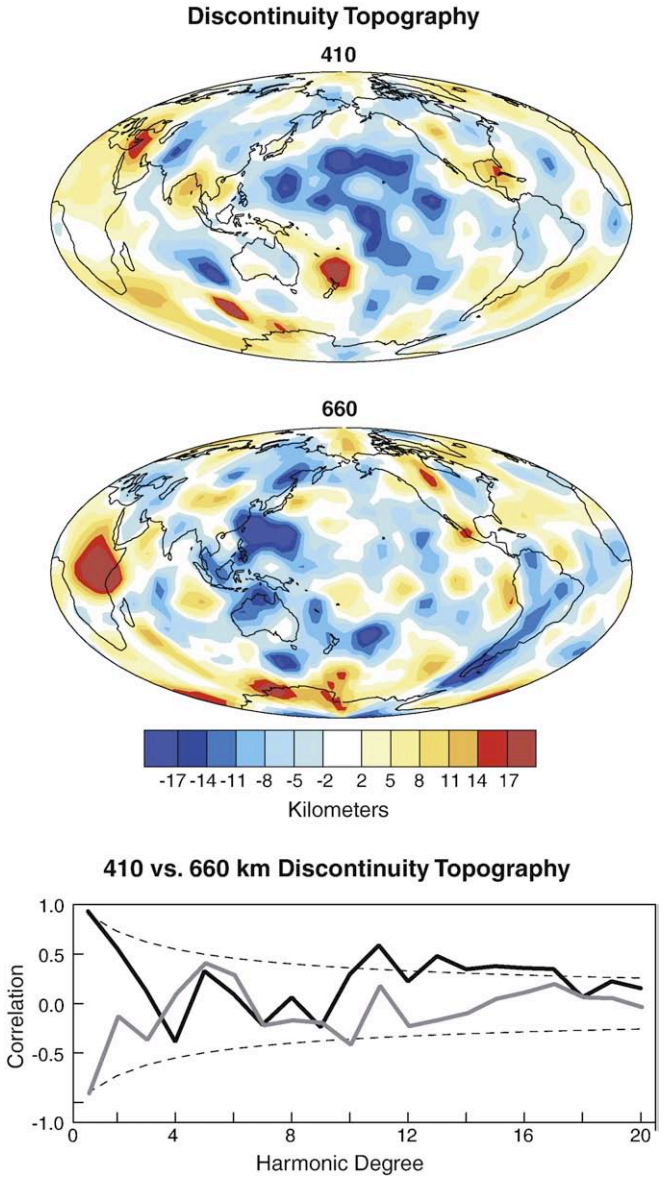

Fig. 2. Deviations from the average 410 and 660 km discontinuity depth corrected for CRUST 2.0 and the 6° shear velocity model described in Houser et al. (2008a). The map is computed using spherical splines which are equivalent to a spherical harmonic expansion out to degree 20. The average depths of the 410 and 660 km discontinuities are 410 km and 650 km respectively, resulting in an average transition zone thickness of 240 km using 20 s PREM. Bottom: blackline, correlation of the above 410 and 660 km discontinuity topography versus harmonic degree. From the expected Clapeyron slopes, the 410 and 660 km discontinuities should be anti-correlated for a vertically coherent thermal anomaly. Grey line, correlation of the discontinuities if the 660 km discontinuity were anti-correlated to the 410 km discontinuity under the Pacific plate. The dashed lines represent the 90% significance level for positive and negative correlations.

Since the topography maps have been corrected for crust and upper mantle structure, it is necessary to evaluate whether features in the topography maps could be due to artifacts associated with these corrections. The application of these corrections and their effects are described in Houser et al. (2008a). The corrections are necessary since the travel time variations from crustal structure and discontinuity

topography are both on the order of a few seconds, and hence the crustal structure could bias the discontinuity depths by 10's of kilometers. To make the crust correction, we determine the two-way travel time through the CRUST 2.0 model (Laske et al., http://mahi.ucsd.edu/Gabi/rem.dir/crust/crust2.html) and subtract it from both the *SS-S410S* and the *SS-S660S* times. Likewise, for the velocity correction, we calculate the predicted two-way travel time anomaly of an *S* wave passing through the upper mantle of the shear velocity model HMSL-S06 (Houser et al., 2008b). Both the *SS-S410S* and the *SS-S660S* times are corrected for upper mantle velocity structure. In addition, the *SS-S660S* times are corrected for velocity anomalies within the transition zone. However, this signal is rather small compared to the topography signal. The Large Low Shear Velocity Provinces (LLSVP) at the base of the mantle have a negligible effect on our results since approximately 95% of our SS waveforms turn above 2100 km depth. The long wavelength features of the recent generation of tomographic models are in relatively good agreement, so the results reported here do not depend strongly on the particular shear velocity model used for the upper mantle and transition zone corrections. The removal of the predicted crust and upper mantle velocity signal will be projected onto the topography of both discontinuities. Thus, regions of anti-correlation or non-correlation are not due to the corrections, despite the Pacific-shaped depression of the 410 km discontinuity.

The shear velocity structure provides the closest approximation to the thermal structure in the transition zone. In the upper mantle, subducting slabs are too narrow to be imaged by the low frequency surface waves used to constrain the upper mantle in many tomographic models, including HMSL-S06. The transition zone of this model is shown in Fig. 3, along with its correlation as a function of harmonic degree with the topography of the 410 and 660 km discontinuities. Fast shear velocities are present under western Africa, the western Pacific, and South America, with the latter two being most likely due to the collection of cold, oceanic lithosphere, although the chemical heterogeneity of the subducting plate can affect shear velocities as well. Slow velocities are found beneath eastern Africa, Eurasia, Antarctica, and the northern Pacific. The lack of correlation between the 410 km discontinuity and tomography led Houser et al. (2008a) to conclude that there may be a chemical effect within that depth range that supersedes the thermal effect. However, comparing the maps in Figs. 2 and 3, it appears that the 410 km discontinuity behavior is not as unusual as that of the 660 km discontinuity outside of subduction zones. Hence, the apparently anomalous behavior is largely confined to the 660 km discontinuity.

The 660 km discontinuity topography has its highest correlation with shear velocity structure at degree two, due to its depression in the western Pacific which is associated with zones of high shear wave speeds, and hence likely cold temperatures. The emergence of high shear wave speeds at the bottom of the transition zone corresponding to the subduction zones in the western Pacific, along with the depression of the 660 km discontinuity, are the main lines of evidence

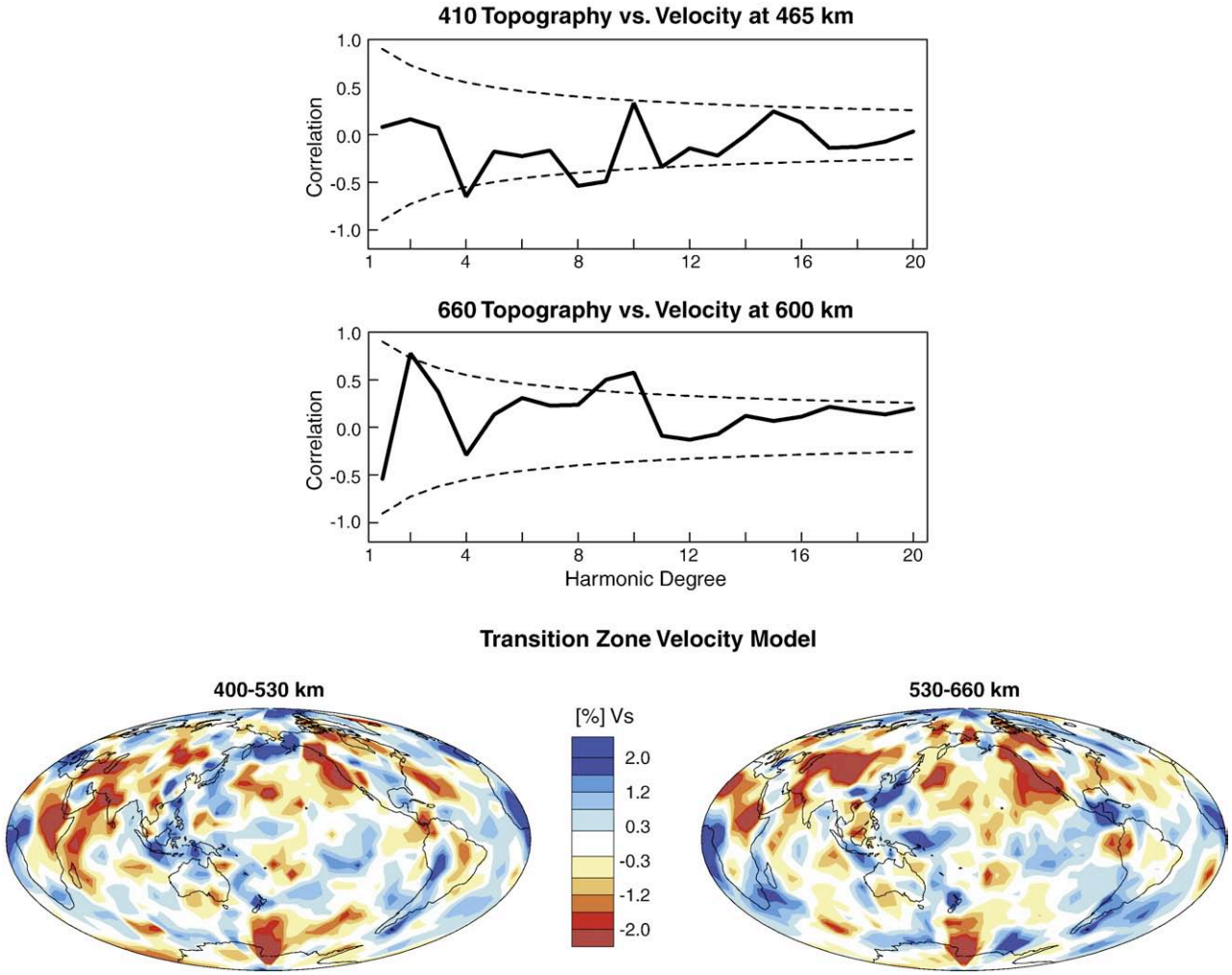

Fig. 3. Top: the correlation of 410 km discontinuity topography and velocity structure in the layer between 400 and 530 km versus harmonic degree. Middle: the correlation of our 660 km discontinuity topography and velocity structure in the layer between 530 and 660 km versus harmonic degree. Bottom: 6° shear velocity model based on Houser et al. (2008b) for layers in the transition zone.

that subducting slabs can reside for extended periods in the transition zone before entering the lower mantle (Fukao et al, 2009). The rise in the 410 km discontinuity in this region is much smaller in amplitude and lateral extent than the depression of the 660 km discontinuity, resulting in a much smaller correlation with velocity at degree two.

The depression of the 410 km discontinuity under the Pacific coincides with the low shear wave velocities that span from Antarctica to the northwest Pacific. This low velocity structure actually is part of a larger low velocity structure that extends from around 350–1000 km depth under the Pacific. The authors are currently investigating the dynamic implications and the 3D structure of this feature. These low shear velocities indicate that the Pacific is underlain by warm material in the transition zone. Thus, the depression of the 410 km discontinuity should, under the standard view of a positive Clapeyron slope for the 410 km discontinuity-forming transition and a negative Clapeyron slope for the 660 km discontinuity-forming transition, be accompanied by a rise in the 660 km discontinuity. However, we observe that the 660 km discontinuity is slightly depressed under the Pacific, with the exception of a few patches which are flat or raised in topography.

In order to better understand the complexities of the discontinuities and associated seismic structures, we have globally mapped the sign of 410 and 660 km discontinuity topography, and correlated these patterns with whether seismic velocity is fast or slow within the transition zone (Fig. 4). The top and bottom maps are views of the western and eastern hemispheres, where each circle represents the relative discontinuity topography from the global average in each 5° bin from Houser et al., (2008a). For instance, a stacked trace that has a shallower than average 410 km discontinuity and a deeper-than-average 660 km discontinuity will plot as dark blue if the seismic velocity is fast, or grey if the seismic velocity is slow. Cool colors are used for fast seismic velocities and warm colors are used for slow seismic velocities. The seismic velocity used is the average of the two layers within the transition zone of the shear model HMSL-S06. The grey regions indicate that neither the 410 nor the 660 km discontinuity are in agreement with the seismic velocity based on a positive Clapeyron slope for the 410 km discontinuity, and a negative Clapeyron slope for the 660 km discontinuity.

While Fig. 4 is complicated, some patterns do emerge. Cool colors dominate the western Pacific and are abundant in the mid-Atlantic and Indian oceans, while warm colors dominate the central Pacific, eastern Africa, and central Eurasia. Dark blue regions represent areas with depressed/elevated 660/410 km discontinuity topography and high shear velocity. Thus, dark blue areas are thought to result from cool oceanic slabs passing through the transition zone causing an anti-correlation of the discontinuity topography. Light blue regions are also found near subduction zones and may be due to slab ponding where the 660 km discontinuity is depressed, but the 410 km discontinuity above it may have been chemically affected by the slab. The orange regions (i.e. the seismic velocity is slow, the 410 km discontinuity is deep, and the 660 km discontinuity is shallow) indicate warm areas where the discontinuity topography agrees with opposite Clapeyron slopes of the two transitions. The dark red regions, with depressed 410 and 660 km discontinuities and slow velocities, are particularly interesting as they seem to be spatially correlated with the orange regions. These red regions imply that the 660 km discontinuity may progress from a negative slope to a positive Clapeyron slope with increasing temperature.

While it is plausible that these complicated seismic observations could be due to lateral variations in chemistry, it is hard to identify one component that can explain them all. For example, the effect of increasing the concentration of hydrogen would be to modestly elevate the 410 km discontinuity (Smyth and Frost, 2002), weakly depress the 660 km discontinuity (Litasov et al., 2005a), and decrease seismic velocities (Jacobsen et al., 2004). However, the low shear velocities under the Pacific in the transition zone are associated with a dramatic depression of the 410 km discontinuity that is not consistent with hydration. In addition, for water concentrations of even as high as

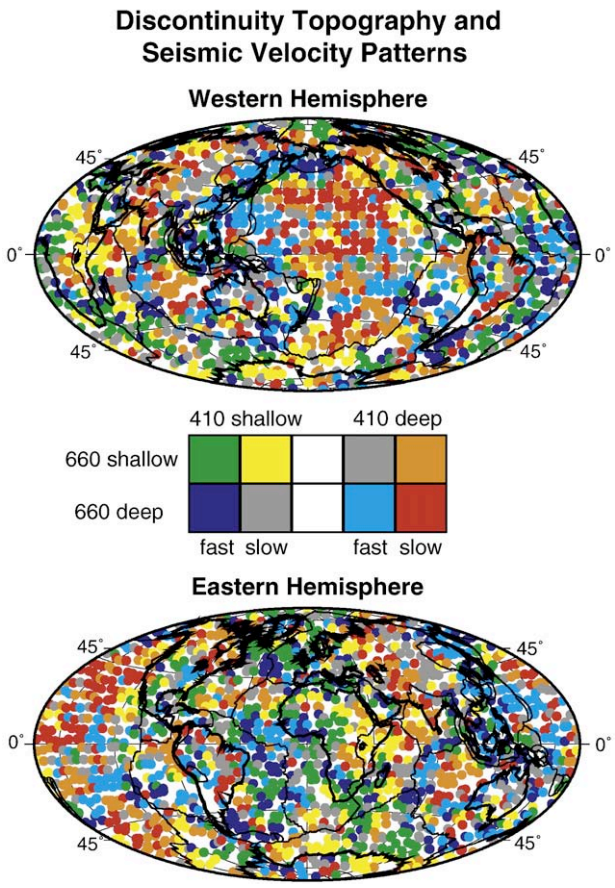

Fig. 4. Maps of the western and eastern hemispheres where each circle represents the relative discontinuity topography from the global average in each 5° bin from Houser et al. (2008a). The color-coding scheme is based on the sign of the seismic velocity anomaly. Cool colors are used for fast seismic velocities and warm colors are used for slow seismic velocities. The grey regions indicate that neither the 410 nor the 660 km discontinuity are in agreement with the seismic velocity based on a positive Clapeyron slope for the 410 km discontinuity and a negative Clapeyron slope for the 660 km discontinuity. White regions are those with little or no coverage.

0.5 wt.%, the changes in discontinuity depth are rather small (~5 km) compared to the large observed values (~15 km). Similarly, the effect of lateral variations of iron content will primarily manifest themselves on the depth of the 410 km discontinuity. Changes in the Fe-number, for example from $Fe_{0.12}$ to $Fe_{0.08}$, within olivine will produce a deepening of ~12 km of the 410 km discontinuity (Akaogi et al., 1989; Katsura and Ito, 1989; Ito and Katsura, 1989). In contrast, the 660 km discontinuity is fairly insensitive to shifts in iron content. However, such a decrease in Fe-number would result in an *increase* in shear velocity while we observe a *decrease* in shear velocity under the Pacific. Hence, there is difficulty reconciling the patterns of the two discontinuities as well as shear velocity with lateral changes in hydrogen or iron content.

The observed shift from anti-correlated phase boundaries to correlated boundaries is likely due to a shift in the dominant phase transformation from the olivine to the garnet system. Therefore, we consider the conditions for which the 660 km discontinuity might have a positive Clapeyron slope. Hirose (2002) found that as temperature increases, majorite becomes progressively more abundant in pyrolitic systems at depths of around 600 km. At temperatures above 1800° C (i.e. 2073 K), the majorite to perovskite transition was observed to occur with a positive Clapeyron slope at pressures corresponding to the 660 km discontinuity. Indeed, Weidner and Wang (1998) showed that as Al content and temperature increase, the majorite to perovskite transition progressively sharpens and becomes larger in amplitude, making it a more effective reflector of seismic energy. Thus, if the slow material in the central Pacific where the red regions are most

concentrated is hot and moderately Al rich (of order 3–5 cation percent Al), the observed energy reflected at depths slightly greater than 660 km could be due to the occurrence of the majorite to perovskite transition at these locations.

3. Transition zone temperatures

In order to compare discontinuity depths with seismic velocities, we have converted both to temperature to determine possible trends and/or correlations between the two datasets. The depths used here were converted from *SS-SdS* times using the predicted travel times for precursor arrivals from PREM (Dziewonski and Anderson, 1981). PREM is then also used to transform discontinuity depth into pressure, with the average temperature for each discontinuity being fixed at the temperature along a geotherm (Brown and Shankland, 1981) for the pressure corresponding to the average depth. This technique provides a reference point from which to evaluate thermal deviations. The pressure difference (dP) is the difference between the depths observed in each cap from the average, and the Clapeyron slope (dP/dT) is then used to find the change in temperature (dT) associated with the observed change in pressure (dP). This temperature change (dT) is then added to the absolute temperature at the average depth from the geotherm to produce an absolute temperature for each bin location. The observed depth of the 410 km and 660 km discontinuities for bins with less than 15 km error in depth are shown in Fig. 5, and the above methodology is used to calculate the predicted temperature variations. Note that this cutoff reduces the number of stacks from 1510 used as the basis of Figs. 2–4 to 1065 bins. The average discontinuity depths/temperatures we use are 410.4 km/1694 K and 650.3 km/1866 K. The Clapeyron slope we use for the 410 km discontinuity is +3.1 MPa/K and the negative

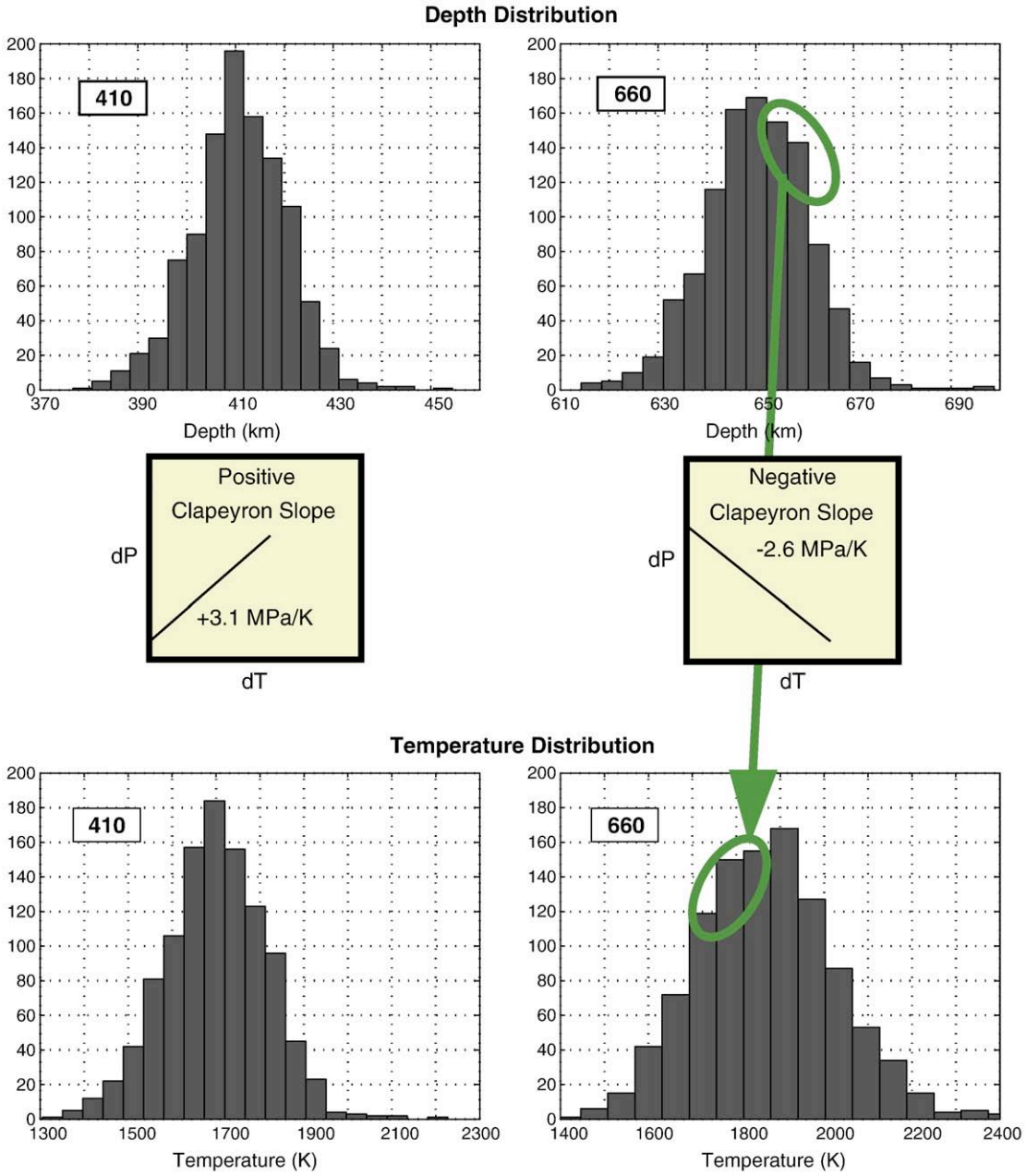

Fig. 5. The observed depth of the 410 km (top left) and 660 km (top right) discontinuities for bins with less than 15 km error in depth. By tying the average depth to the temperature predicted using the Brown and Shankland (1981) geotherm and a positive Clapeyron slope for the 410 km discontinuity and a negative slope for the 660 km discontinuity, we can predict the temperature variations associated with the observed depth variations. Note that the lobe of deeper-than-average 660 km discontinuity observation maps into colder-than-average temperatures.

Clapeyron slope we use for the 660 km discontinuity is −2.6 MPa/K (Akaogi et al., 2007).

However, we also evaluate the effects of different Clapeyron slopes on our inferred temperature distributions: this is motivated by the range in reported Clapeyron slopes for the perovskite-forming reaction; −3.0 MPa/K (Ito and Takahashi, 1989; Irifune et al., 1998), −2.0 to −0.4 (Katsura et al., 2003), −1.3 MPa/K (Fei et al., 2004), −0.8 to −0.2 MPa/K (Litasov et al., 2005b). Fig. 6 demonstrates what happens to the temperature distribution as the Clapeyron slope of the perovskite-forming reaction changes between −0.5 and −3.0 MPa/K. As the Clapeyron slope approaches zero, the temperature fluctuations necessary to explain the observed depth variations become, as expected, unrealistically high. However, even for a value of −1.5 MPa/K, the temperature variation is around 1000 K: a range markedly higher than the 300–500 K range usually inferred from geodynamic models (Simmons et al., 2009). The error associated with the observed discontinuity topography and thus in the predicted temperatures (Figs. 5, 8, 9, 10) is provided in Fig. 7. Most bins have a 3 km error in the measured discontinuity depth which translates to a temperature around 60 K. Since the following analyses focus on the overall form of the predicted temperature distributions, errors on the individual measurements will not have a significant impact on these patterns.

Fig. 8 shows the distribution of temperatures derived from the 660 km discontinuity depths (grey) for different crossover temperatures for the transition from the negative Clapeyron slope to the positive Clapeyron slope for the 660 km discontinuity. with a positive slope of +1.5 MPa/K (Hirose, 2002) at high temperatures. Our rationale for using different crossover temperatures is simply because of the well-known kinetic effects on garnet destabilization: in this instance the experimental bound is likely an upper estimate of the true pressure of the transition (Nishiyama and Yagi, 2003; Kubo et al., 2008). We started with the experimentally determined value of 2073 K and stepped down by 50 K until 1873 K where we approach the average predicted temperatures for the 660 km discontinuity. Whether the 660 km discontinuity is above or below the crossover temperature is determined by the adiabatic extrapolation of temperature from that predicted by the 410 km discontinuity topography at that bin location.

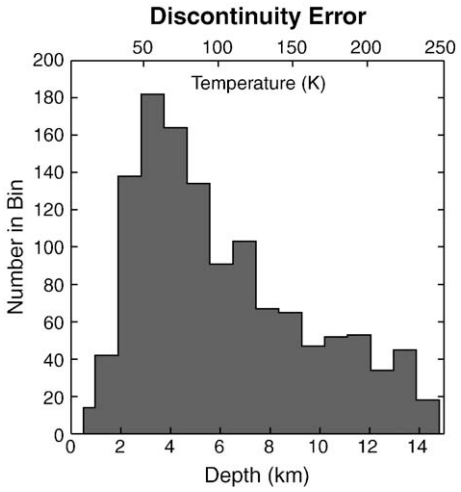

Fig. 7. Histogram of the measurement error of 410 km and 660 km discontinuity depth used as the basis for Figs. 5, 8, 9, and 10, i.e. those with errors less than 15 km. The bottom axis is the depth error and the top axis is the associated error in the predicted temperature assuming a Clapeyron slope with a magnitude of 2.5 MPa/K.

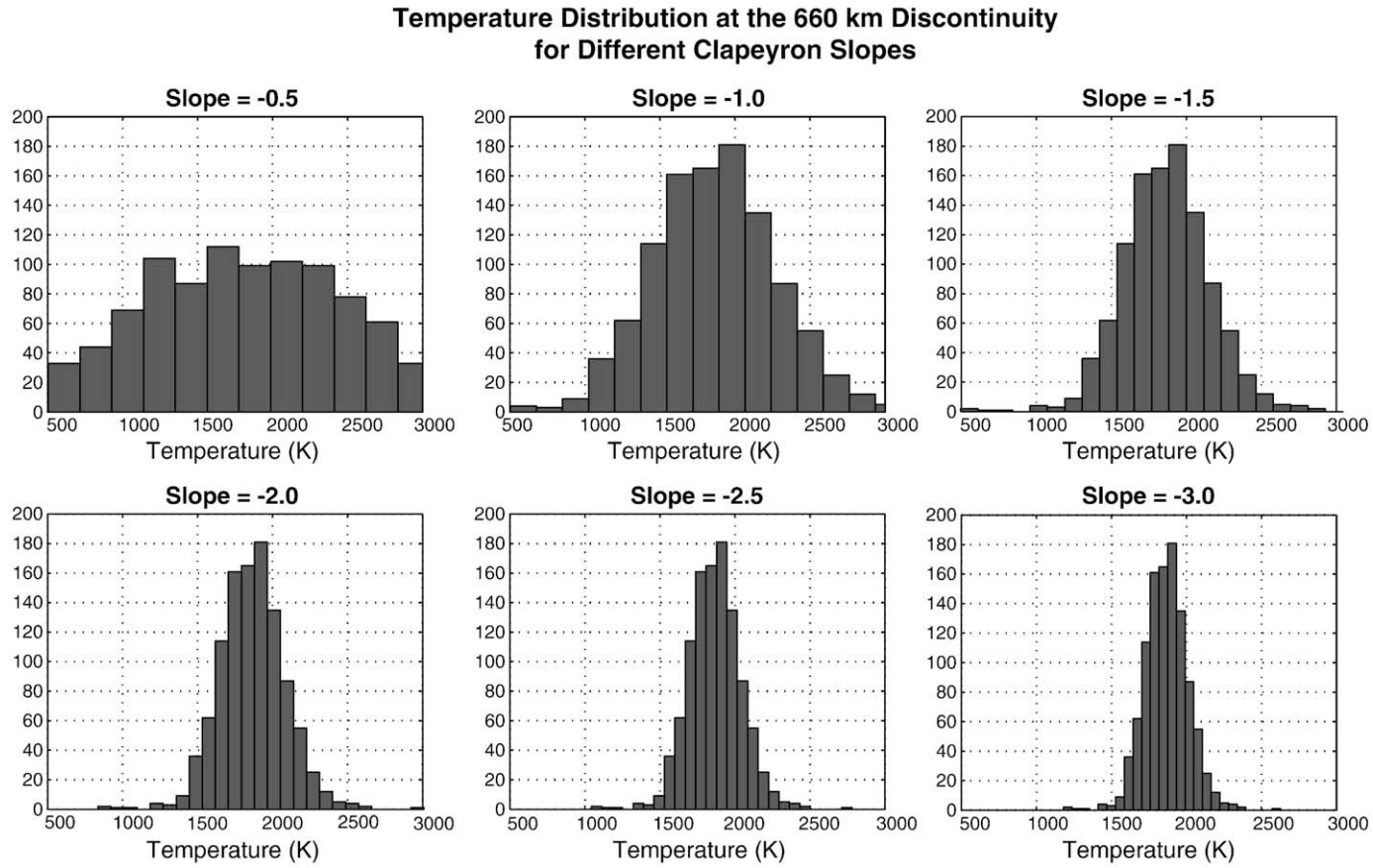

Fig. 6. Histograms of the temperature distributions at the 660 km discontinuity assuming different Clapeyron slopes. As the Clapeyron slope falls below 1 MPa/K, the temperature fluctuations necessary to explain the observed depth variations become unrealistically high. As the Clapeyron slope increases, the temperature fluctuations become increasingly narrow. The negative Clapeyron slope we use for Figs. 7–9 is −2.6 MPa/K from Akaogi et al. (2007) and the positive slope is +1.5 MPa/K from Hirose (2002).

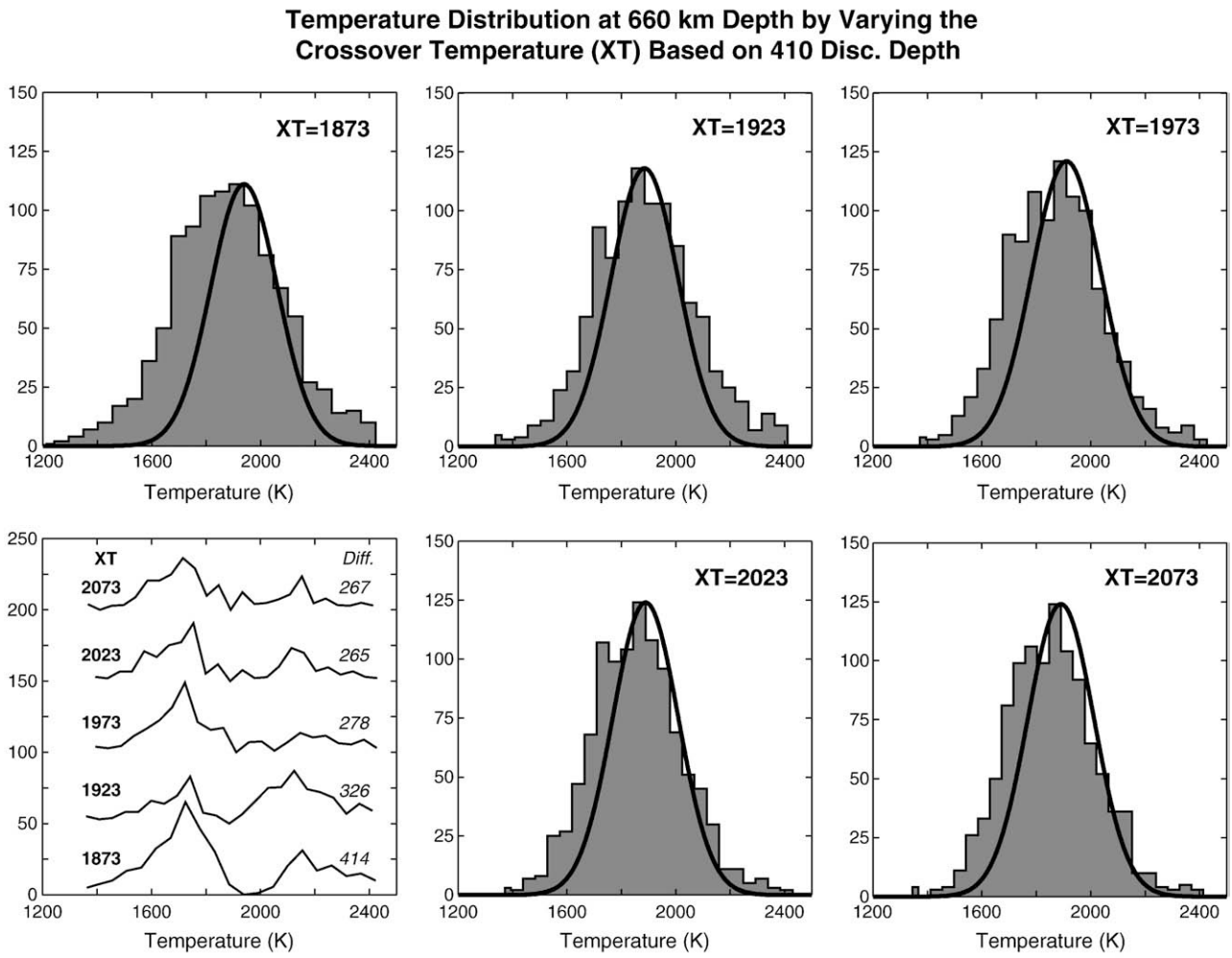

Fig. 8. Histograms of temperatures calculated from the observed depths of the 660 km discontinuity depths (grey). Here the depth of the 410 km discontinuity has been used to determine which locations exceed the crossover temperature (XT). We use a positive Clapeyron slope for the bins that exceed this crossover temperature. The Gaussian distribution of the temperatures from the 410 km discontinuity is shown by the solid black line, having been shifted to align with the peak temperature from the 660 km discontinuity depths and broadened to compensate for the differences in the magnitude of the Clapeyron slopes. The absolute value of the difference between the distribution of temperatures from the 660 km discontinuity and the Gaussian distribution from the 410 km discontinuity is shown in the bottom left graph for each crossover temperature. The sum of the difference curve is provided on the right side of the graph. Note: each difference curve has been offset by 50 for plotting. The crossover temperature from a negative to positive Clapeyron slope occurs between 1923 K and 2073 K. See text for Clapeyron slopes and geotherms used.

Thus, where the 410 km discontinuity is shallow, the 660 km discontinuity will be predicted to be cool, and regions where the 410 km discontinuity is depressed, the 660 km discontinuity will be predicted to be warm.

The histograms for the temperature at the 660 km discontinuity using 2073 K as the crossover temperature between a negative and positive Clapeyron slope are skewed to low temperatures, whereas the temperatures from the 410 km discontinuity have a more Gaussian distribution (Fig. 8). To demonstrate this, we have plotted the Gaussian distribution of temperature predicted from the observed 410 km discontinuity depths (dark black line) on top of the predicted 660 km discontinuity temperatures. The distribution has been aligned with the peak in the 660 km discontinuity temperatures and has been broadened to compensate for the differences in the magnitude of the Clapeyron slopes of the two discontinuities. Obviously, the temperature range broadens as the magnitude of the Clapeyron slope decreases (Fig. 6). The usage of two Clapeyron slopes allows the low temperature skew of the 660 km discontinuity temperatures to be reduced; a far closer resemblance between the 410 and 660 km discontinuity derived temperature distributions is produced using a crossover temperature that is greater than ~1923 K. The low temperature skew is particularly pronounced in the Pacific, where we observe patches of depressed 660 km discontinuity depths where both the 410 km discontinuity topography and seismic velocities indicate that the region is warm. If a positive Clapeyron slope is used to evaluate the temperature of these patches, then the distribution of temperatures from the 660 km discontinuity becomes more Gaussian, and thus more similar to that of the 410 km discontinuity. While it is difficult to pinpoint the precise crossover temperature, it does appear to be between 1920 K and 2020 K. The 2073 K value of the crossover temperature found by (Hirose, 2002) is on the very highest end of what we expect for an adiabatic transition zone, and thus this crossover temperature only affects a handful of bins. In order for the change in the sign of the Clapeyron slope of the 660 km discontinuity to reduce the skew of the seismic observations, we find that the crossover temperature would need to be 50–150 K lower than that observed experimentally.

This optimal crossover temperature is, however, empirical and the question arises of whether there are other means to assess whether a positive or negative Clapeyron slope may be more appropriate for the 660 km discontinuity-forming transition in a given area. To test the robustness of our result, we applied another method of determining whether a positive or negative Clapeyron slope should be used. We convert the shear velocity model HMSL-S06 to temperature using an approximate sensitivity of shear velocity to temperature (dlnVs/dT) of

transition zone minerals of -7×10^{-5}/K (Stixrude and Lithgow-Bertelloni, 2005). To be consistent, the average discontinuity depths are again used as the temperature tie points. In Fig. 9, the temperatures from the 660 km discontinuity are calculated in the same way as in Fig. 8. However, whether a positive or negative Clapeyron slope is applied to the temperatures of the 660 km discontinuity is determined by the inferred temperature above 660 km depth from the tomographic shear velocity anomalies. The patterns of Fig. 9 are very similar to those of Fig. 8, and both methods find that the distribution of temperatures at the 660 km discontinuity most closely resembles those from the 410 km discontinuity near ~1923 K.

The distribution of temperatures from the 660 km discontinuity for both methods using a crossover temperature of 2073 K might seem reasonable given that subducting slabs are likely ponding at this depth and cooling large regions of the discontinuity relative to the 410 km discontinuity. There are very few bins in which either the 410 km discontinuity topography or the seismic velocity predict temperatures exceeding 2073 K at the 660 km depth. Therefore, there is very little effect on the distributions assuming a change in the Clapeyron slope for the 660 km discontinuity at 2073 K. Since shallow 410 discontinuity topography and fast shear velocities occur within most subduction zones, both methods will predict cool temperatures for the 660 km discontinuity topography in these regions. The skewness arises from depressions of the 660 km discontinuity from both areas of subduction as well as beneath the Pacific plate, which maps to cold temperatures. As the crossover temperature decreases, the depressions of the 660 km discontinuity in the Pacific get mapped into higher temperatures, thus removing the skewness of the 660 km temperature distribution towards colder temperatures. The observations that both the 410 km discontinuity topography and the shear velocities under the Pacific indicate warmer temperatures, and our demonstration that the skewness of the temperature distribution at 660 km is due to the depression of the 660 km discontinuity under the Pacific provide strong evidence that the seismically observed reflections near 660 km under much of the Pacific are a consequence of the majorite to perovskite transition.

Since a major contribution to the observed correlation of 410 and 660 km discontinuity topography appears to occur under the Pacific ocean, we plot the distributions of our inferred temperatures underneath oceans and continents separately. Since oceans cover a majority of the Earth's surface, and the best resolved *SS* stacks occur under the northwest Pacific, there are many more bins under oceans than continents. In Fig. 10, we show the distributions from both methods for crossover temperatures of 2073 K and 1923 K. We use ETOPO2v2 2006 downloaded from the National Geophysical Data Center (http://www.ngdc.noaa.gov/mgg/fliers/06mgg01.html) evaluated at 10 minute

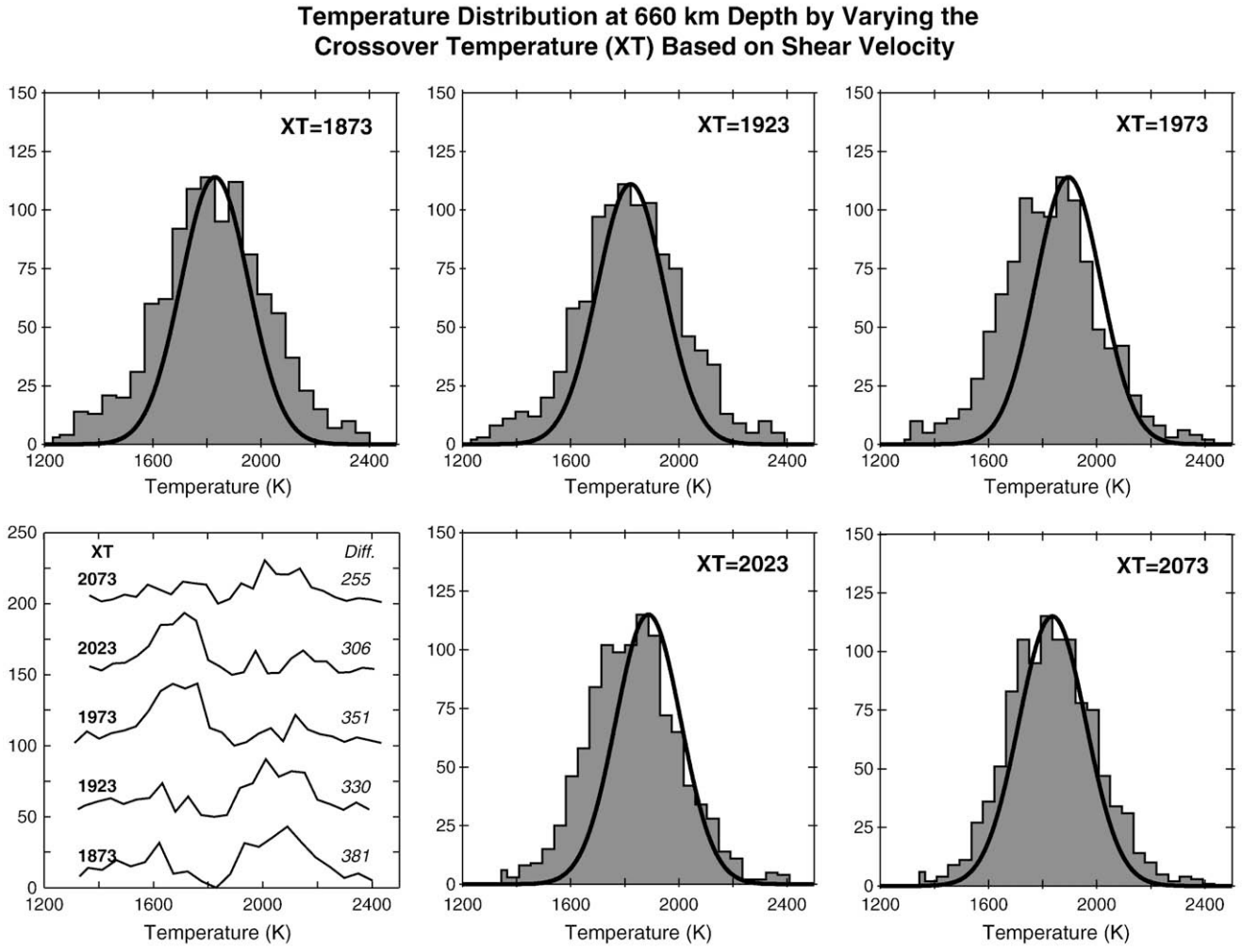

Fig. 9. Histograms of temperatures calculated from the observed depths of the 660 km discontinuity depth (grey). Here the shear velocity model HMSL-S06 in the transition zone has been used to determine which locations exceed the crossover temperature (XT). We use a positive Clapeyron slope for the bins that exceed this crossover temperature. The Gaussian distribution of the temperatures from the 410 km discontinuity is shown by the solid black line, which has been shifted to align with the peak temperature from the 660 km discontinuity depths. The distribution of temperatures at 660 km depth matches the distribution at 410 km depth best when the crossover temperature from a negative to positive Clapeyron slope occurs between 1923 K and 2023 K. See text for Clapeyron slopes and geotherms used.

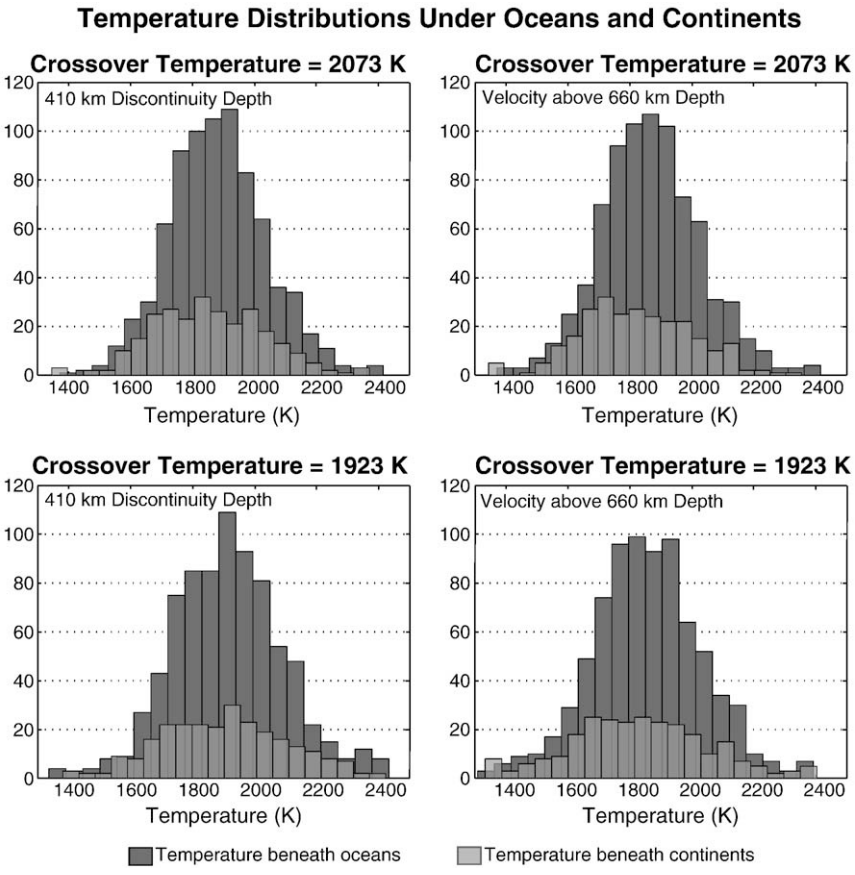

Fig. 10. Histograms of temperatures underneath oceans (dark grey) and continents (translucent grey) calculated in the same way as for Figs. 5 and 6 for crossover temperatures of 2073 K (top row) and 1923 K (bottom row). The left column uses the depths of the 410 km discontinuity (i.e. Fig. 8) and the right column uses shear velocity (i.e. Fig. 9) as a proxy for temperature at the 660 km depth. The distribution of temperatures at 660 km depth is less skewed to lower temperatures when the crossover temperature from a negative to positive Clapeyron slope occurs around 1923 K rather than 2073 K. Lowering the crossover temperature has the largest effect on the distribution of temperatures under oceans based on observed depths of the 660 km discontinuity. See text for Clapeyron slopes and geotherms used.

intervals to assess whether a bin is in an oceanic or continental region. The distributions of the temperatures beneath the oceans are more similar to the temperature distributions from the 410 km discontinuity (Figs. 8, 9) than the distributions beneath the continents using both methods. However, there are few continental bins from which to define a distribution trend. The greatest improvement in the correlation between the temperature distribution around 410 km depth and either the oceans or continents occurs under oceans using the method in which the depth of the 410 km discontinuity is used to extrapolate temperatures down to the 660 km discontinuity, for a crossover temperature greater than 1923 K. This indicates that the depth of the 410 km discontinuity may be a better proxy for temperatures at the 660 km discontinuity than temperatures derived from seismic velocities, although the agreement between the two methods is quite notable. The main conclusion that can be drawn by separating the distributions beneath oceans and continents is that the distribution of temperatures under the oceans is more dramatically affected by reducing the crossover temperature than the broader distributions observed under continents.

A superadiabatic geotherm could reduce the discrepancy between the experimental observations (Hirose, 2002) and the seismic observations presented here. The absolute temperature of the crossover from a negative to positive Clapeyron slope depends mostly on the chosen geotherm, similar to absolute discontinuity depth being dominated by the 1D velocity model. The (Brown and Shankland, 1981) geotherm used here is simply an adiabat; without any non-adiabatic gradients at different depths. Thus, it is essentially a one-layer mantle geotherm, and could be too low in transition zone if there is a thermal boundary layer somewhere above the 660 km discontinuity. All higher-temperature geotherms result from small superadiabatic gradients within the transition zone, or temperatures that, when extrapolated to shallow depths, somewhat exceed the conditions of basaltic petrogenesis. Therefore, higher temperatures than those used here may be present in the transition zone if there are superadiabatic gradients somewhere below the depth of basalt petrogenesis, otherwise, (Brown and Shankland, 1981) is likely within ≈50 K of the Earth's geotherm.

Recent work has also found higher temperatures in the transition zone in the area around Pacific hot spots (Courtier et al., 2007b; Ritsema et al., 2009). The global maps of transition zone thickness from *SS* precursors all show that the transition zone is thinner than average under the Pacific. This is in agreement with regional studies of Pacific hot spots that find the transition zone is most often thinner than average (Suetsugu et al., 2004; Schmerr and Garnero, 2006; Courtier et al., 2007a) and that shear velocities are low (Zhao, 2007).However, since the transition zone is thin throughout the Pacific, the interpretation of separate, localized thermal anomalies leading to each hot spot may instead reflect a warmer basin-wide thermal structure. Studies have attempted to systematically look at *SS* precursors under hot spots and have found similar results to those here, in that many hot spots exhibit depressed 410 and 660 km discontinuities (Deuss, 2007; Gu et al., 2009). Both of these studies suggest that the majorite to perovskite transition might explain the observations, but reconciling the depth observations with the mineral physics results (e.g. determining a consistent crossover temperature) has not been conducted. Directly resolving both the ringwoodite–majorite and majorite–perovskite seismic reflections (pressure difference 1 GPa≈26 km) is below the resolution of long-

period SS waves. Indeed, our results are suggestive that the crossover point for a negative to positive Clapeyron slope for the main perovskite-forming reaction in an Al-enriched pyrolite composition may be experimentally overestimated by up to ~150 K. That is to say, if the actual crossover temperature from the ringwoodite-to-perovskite to the majorite to perovskite transition is not lower than the currently observed value of 2073 K, then this mechanism cannot explain the seismic observations of discontinuity correlations under warm regions.

4. Conclusion

We have utilized the data of Houser et al. (2008a) to examine the global correlation between the depths of the 410 and 660 km discontinuities. This correlation is due in large part to a slight correlation or lack of correlation between the 410 and 660 km discontinuities under the Pacific plate. By mapping out the pattern of discontinuity depths and seismic velocities in the transition zone, we find that the pattern of correlation between the 410 and 660 km discontinuities is rather complicated, but that both the 410 km discontinuity depths and seismic velocities indicate that high temperatures are present under the Pacific. By converting the discontinuity depths to temperatures using a single, negative Clapeyron slope for the perovskite-forming reaction, we observe a skewness in the distribution of temperatures from the 660 km discontinuity that is not observed in the temperatures from the 410 km discontinuity. This discrepancy is reduced if a positive Clapeyron slope is applied to the 660 km discontinuity at temperatures greater than 1923 K, using both the 410 km discontinuity and shear velocity as a proxy for temperature at 660 km depth. This shift in slope is in accord with multi-anvil press observations of the perovskite-forming reaction in pyrolite at high temperatures (Hirose, 2002). The temperature that we infer for the change in the sign of the slope is up to 150 K lower than is observed in experiments: we attribute this to the well-known kinetic effects on garnet destabilization reactions (Nishiyama and Yagi, 2003; Kubo et al., 2008). Hence, if the majorite to perovskite transition does not actually occur at temperatures much lower than what has been determined so far experimentally, then another mechanism is needed to reconcile the correlation of the 410 and 660 km discontinuities in seismically slow regions. The dominance of the majorite to perovskite reaction is anticipated in fertile, Al rich mantle at high temperatures, and is thus compatible with the sub-Pacific being a zone characterized by upwelling geochemically enriched mantle. Furthermore, values of the Clapeyron slope of −2.6 MPa/K for the lower temperature portion of the perovskite-forming reaction produce geodynamically plausible lateral temperature variations. Proposed values as low as −0.5 MPa/K produce temperature variations well in excess of 1000 K.

Acknowledgments

Work supported by the US National Science Foundation, including grant EAR062985 of the Cooperative Studies of the Earth's Deep Interior (CSEDI) program. The data were acquired using the IRIS Data Management Center which is funded through the Instrumentation and Facilities Program of the NSF EAR-0004370. Specific networks include, but are not limited to, GEOSCOPE, IDA, MEDNET, GEOFON, PACIFIC21, and those from the USGS. We thank the two anonymous reviewers for constructive comments that considerably improved the original manuscript.

References

Ai, Y., Zheng, T., Xu, W., He, Y., Dong, D., 2003. A complex 660 km discontinuity beneath northwestern China. Earth Planet. Sci. Lett. 212, 63–71.

Akaogi, M., Ito, E., Navrotsky, A., 1989. Olivine-modified spinel–spinel transitions in the system Mg_2SiO_4–Fe_2SiO_4: calorimetric measurements, thermochemical calculation, and geophysical application. J. Geophys. Res. 94, 15671–15685.

Akaogi, M., Takayama, H., Kojitani, H., Kawaji, H., Atake, T., 2007. Low-temperature heat capacities, entropies and enthalpies of Mg_2SiO_4 polymorphs, and $\alpha-\beta-\gamma$ and post-spinel phase relations at high pressure. Phys. Chem. Miner. 34, 169–183. doi:10.1007/s00269-006-0137-3.

Anderson, D., 1967. Phase changes in the upper mantle. Science 157, 1165–1173.

Benoit, M., Nyblade, A., Owens, T., Stuart, G., 2006. Mantle transition zone structure and upper mantle S velocity variations beneath Ethiopia: evidence for a broad, deep-seated thermal anomaly. Geochem. Geophys. Geosys. 7. doi:10.1029/2006GC001398.

Bostock, M., 1996. *Ps* conversions from the upper mantle transition zone beneath the Canadian landmass. J. Geophys. Res. 101, 8393–8402.

Brown, J., Shankland, T., 1981. Thermodynamic parameters in the Earth as determined from seismic profiles. Geophys. J. R. Astron. Soc. 66, 579–596.

Chambers, K., Woodhouse, J., Deuss, A., 2005. Topography of the 410 km discontinuity from *PP* and *SS* precursors. Earth Planet. Sci. Lett. 235, 610–622.

Chevrot, S., Vinnik, L., Montagner, J.-P., 1999. Global-scale analysis of the mantle *Pds* phases. J. Geophys. Res. 104, 20203–20219.

Collier, J., Helffrich, G., Wood, B., 2001. Seismic discontinuities in subduction zones. Phys. Earth Planet. Int. 127, 39–49.

Courtier, A., Bagley, B., Revenaugh, J., 2007a. Whole mantle discontinuity structure beneath Hawaii. Geophys. Res. Lett. 34, L17304. doi:10.1029/2007GL031006.

Courtier, A., Jackson, M., Lawrence, J., Wang, Z., Lee, C.-T.A., Halama, R., Warren, J., Workman, R., Xu, W., Hirschmann, M., Larson, A., Hart, S., Stixrude, L., Lithgow-Bertelloni, C., Chen, W.-P., 2007b. Correlation of seismic and petrologic thermometers suggests deep thermal anomalies beneath hotspots. Earth Planet. Sci. Lett. 264, 308–316.

Deuss, A, 2007. Seismic observations of transition zone discontinuities beneath hotspot locations. In: Foulger, G., Jurdy, D (Eds.), Plates, Plumes and Planetary Processes, Vol. 430. Geological Society of America, pp. 121–136.

Dziewonski, A., Anderson, D., 1981. Preliminary reference Earth model. Phys. Earth Planet. Int. 25, 297–356.

Fei, Y., Orman, J., Li, J., Westrenen, W., Sanloup, C., Minarik, W., Hirose, K., Komabayashi, T., Walter, M., Funakoshi, K., 2004. Experimentally determined postspinel transformation boundary in Mg_2SiO_4 using MgO as an internal pressure standard and its geophysical implications. J. Geophys. Res. 109, B2305. doi:10.1029/2003JB002562.

Flanagan, M., Shearer, P., 1998. Global mapping of topography on transition zone discontinuities by stacking of *SS* precursors. J. Geophys. Res. 103, 2673–2692.

Flanagan, M., Shearer, P., 1999. A map of topography on the 410-km discontinuity from *PP* precursors. Geophys. Res. Lett. 26, 549–552.

Fukao, Y., Obayashi, M., Nakakuki, T., The Deep Slab Project Group, 2009. Stagnant slab: a review. Annu. Rev. Earth Planet. Sci. 37, 19–46.

Gu, Y., An, Y., Sacchi, M, Schultz, R, Ritsema, J., 2009. Mantle reflectivity structures beneath oceanic hotspots. Geophys. J. Int. in revision, 000–000.

Gu, Y., Dziewonski, A., Agee, C., 1998. Global de-correlation of the topography of transition zone discontinuities. Earth Planet. Sci. Lett. 157, 57–67.

Gu, Y., Dziewonski, A., Ekstrom, G., 2003. Simultaneous inversion for mantle shear velocity and topography of transition zone discontinuities. Geophys. J. Int. 154, 559–583.

Helffrich, G., 2000. Topography of the transition zone seismic discontinuities. Rev. Geophys. 38, 141–158.

Hirose, K., 2002. Phase transitions in pyrolitic mantle around 670-km depth: implications for upwelling of plumes from the lower mantle. J. Geophys. Res. 107. doi:10.1029/2001JB000597.

Hooft, E., Toomey, D., Solomon, S., 2003. Anomalously thin transition zone beneath the Galapagos hotspot. Earth Planet. Sci. Lett. 216, 55–64.

Houser, C., Masters, G., Flanagan, M., Shearer, P., 2008a. Determination and analysis of long-wavelength transition zone structure using *SS* precursors. Geophys. J. Int. 174, 178–194.

Houser, C., Masters, G., Shearer, P., Laske, G., 2008b. Shear and compressional velocity models of the mantle from cluster analysis of long-period waveforms. Geophys. J. Int. 174, 195–212.

Irifune, T., Nishiyama, N., Kuroda, K., Inoue, T., Isshiki, M., Utsumi, W., Funakoshi, K., Urakawa, S., Uchica, T., Katsura, T., Ohtaka, O., 1998. The postspinel phase boundary in Mg_2SiO_4 determined by in situ X-ray diffraction. Science 279, 1698–1700.

Ita, J., Stixrude, L., 1992. Petrology, elasticity, and composition of the mantle transition zone. J. Geophys. Res. 97, 6849–6866.

Ito, E., Katsura, T., 1989. A temperature profile of the mantle transition zone. Geophys. Res. Lett. 16, 425–428.

Ito, E., Takahashi, E., 1989. Post-spinel transformation in the system $MgSiO_3$–Fe_2SiO_4 and some geophysical implications. J. Geophys. Res. 94, 10637–10646.

Jacobsen, S., Smyth, J., Spetzler, H., Holl, C., Frost, D., 2004. Sound velocities and elastic constants of iron-bearing hydrous ringwoodite. Phys. Earth Planet. Int. 143–144, 47–56.

Jeffreys, H., Bullen, K., 1940. Seismological Tables. British Assoc. Adv, Sci.

Katsura, T., Ito, E., 1989. The system Mg_2SiO_4–Fe_2SiO_4 at high pressures and temperatures' precise determination of stabilities of olivine, modified spinel, and spinel. J. Geophys. Res. 94, 15663–15670.

Katsura, T, Yamada, H., Kubo, A., Shinmei, T., Nishikawa, O., Yoshino, T., Aizawa, Y., s. Song, M, Walter, M, Ito, E., Funakoshi, K, 2004. Olivine–wadsleyite transition in the system $(Mg,Fe)_2SiO_4$. J. Geophys. Res. 109. doi:10.1029/2003JB002438.

Katsura, T., Yamada, H., Shinmei, T., Kubo, A., Ono, S., Kanzaki, M., Yoneda, A., Walter, M., Ito, E., Urakawa, S., Funakoshi, K., Utsumi, W., 2003. Post-spinel transition in Mg_2SiO_4 determined by high P–T in situ X-ray diffractometry. Phys. Earth Planet. Int. 136, 11–24.

Kubo, T., Ohtani, E., Kato, T., Kondo, T., Hosoya, T., Sano, A., Kikegawa, T., 2008. Kinetics of the post-garnet transformation: implications for density and rheology of subducting slabs. Phys. Earth Planet. Int. 170, 181–192.
Langston, C., 1979. Structure under Mount Rainier, Washington, inferred from teleseismic body waves. J. Geophys. Res. 84, 4749–4762.
Lawrence, J., Shearer, P., 2006a. Constraining seismic velocity and density for the mantle transition zone with reflected and transmitted waveforms. Geochem. Geophys. and Geosyst. 7. doi:10.1029/2006GC001339.
Lawrence, J., Shearer, P., 2006b. A global study of transition zone thickness using receiver functions. J. Geophys. Res. 111. doi:10.1029/2005JB003973.
Lawrence, J., Shearer, P., 2008. Imaging mantle transition zone thickness with *SdS-SS* finite-frequency sensitivity kernels. Geophys. J. Int. 174, 143–158.
Lebedev, S., Chevrot, S., van der Hilst, R., 2002. The 660-km discontinuity within the subducting NW-Pacific lithospheric slab. Earth Planet. Sci. Lett. 205, 25–35.
Lebedev, S., Chevrot, S., van der Hilst, R., 2003. Correlation between the shear-speed structure and thickness of the mantle transition zone. Phys. Earth Planet. Int. 136, 25–40.
Li, X., Kind, R., Sobolev, S., Tilmann, F., Yuan, X., Weber, M., 2000a. Mapping the Hawaiian plume conduit with converted seismic waves. Nature 405, 938–941.
Li, X., Kind, R., Yuan, X., Sobolev, S., Hanks, W., Ramesh, D., Gu, Y., Dziewonski, A., 2003. Seismic observation of narrow plumes in the oceanic upper mantle. Geophys. Res. Lett. 30. doi:10.1029/2002GL015411.
Li, X., Sobolev, S., Kind, R., Yuan, X., Estabrook, C., 2000b. A detailed receiver function image of the upper mantle discontinuities in the Japan subduction zone. Earth Planet. Sci. Lett. 183, 527–541.
Litasov, K., Ohtani, E., Sano, A., Suzuki, A., 2005a. Wet subduction versus cold subduction. Geophys. Res. Lett. 32. doi:10.1029/2005GL022921.
Litasov, K., Ohtani, E., Sano, A., Suzuki, A., Funakoshi, K., 2005b. In situ X-ray diffraction study of post-spinel transformation in a peridotite mantle: implication for the 660-km discontinuity. Earth Planet. Sci. Lett. 238, 311–328.
Nishiyama, N., Yagi, T., 2003. Phase relation and mineral chemistry in pyrolite to 2200 °C under the lower mantle pressures and implications for dynamics of mantle plumes. J. Geophys. Res. 108. doi:10.1029/2002JB002216.
Nyblade, A., Knox, R., Gurrola, H., 2000. Mantle transition zone thickness beneath Afar: implications for the origin of the Afar hotspot. Geophys. J. Int. 142, 615–619.
Owens, T., Nyblade, A., Gurrola, H., Langston, C., 2000. Mantle transition zone structure beneath Tanzania, East Africa. Geophys. Res. Lett. 27, 827–830.
Parker, R, 1994. Geophysical Inverse Theory. Princeton University Press.
Ramesh, D., Kawakatsu, H., Watada, S., Yuan, X., 2005. Receiver function images of the central Chugoku region in the Japanese islands using Hi-net data. Earth Planets Space 57, 271–280.
Ramesh, D., Kind, R., Yuan, X., 2002. Receiver function analysis of the North American crust and upper mantle. Geophys. J. Int. 150, 91–108.
Revenaugh, J., Jordan, T., 1991. Mantle layering from *ScS* reverberations; 2, the transition zone. J. Geophys. Res. 96, 19763–19780.
Ritsema, J., Cupillard, P., Tauzin, B., Xu, W., Stixrude, L., Lithgow-Bertelloni, C., 2009. Joint mineral physics and seismic wave travel time analysis of upper mantle temperature. Geology 37, 363–366.
Saita, T., Suetsugu, D., Ohtaki, T., Takenaka, H., Kanjo, K., Purwana, I., 2002. Transition zone thickness beneath Indonesia as inferred using the receiver function method for data from JISNET regional broadband seismic network. Geophys. Res. Lett. 29. doi:10.1029/2001GL013629.
Schmerr, N., Garnero, E., 2006. Investigation of upper mantle discontinuity structure beneath the central Pacific using *SS* precursors. J. Geophys. Res. 111. doi:10.1029/2005JB004197.
Schmerr, N., Garnero, E., 2007. Upper mantle discontinuity topography from thermal and chemical heterogeneity. Science 318, 623–626.
Shearer, P., 1991. Constraints on upper mantle discontinuities from observations of long-period reflected and converted phases. J. Geophys. Res. 96, 18182–18187.
Shearer, P., 1993. Global mapping of upper mantle reflectors from long-period *SS* precursors. Geophys. J. Int. 115, 878–904.
Shearer, P, 2000. Upper mantle seismic discontinuities. In: Karato, S, Forte, A., Liebermann, R., Masters, G., Stixrude, L. (Eds.), Earth's Deep Interior: Mineral Physics and Tomography from the Atomic to Global Scale. American Geophysical Union Monograph, pp. 115–131.
Shearer, P., Flanagan, M., 1999. Seismic velocity and density jumps across the 410- and 660-kilometer discontinuities. Science 285, 1545–1548.
Shearer, P., Masters, G., 1992. Global mapping of topography on the 660-km discontinuity. Nature 355, 791–796.
Shen, Y., Solomon, S., Bjarnason, I., Wolfe, C., 1998. Seismic evidence for a lower-mantle origin of the Iceland plume. Nature 395, 62–65.
Simmons, N., Forte, A., Grand, S., 2009. Joint seismic, geodynamic and mineral physical constraints on three-dimensional mantle heterogeneity: implications for the relative importance of thermal versus compositional heterogeneity. Geophys. J. Int. 177, 1284–1304.
Smyth, J., Frost, D., 2002. The effect of water on the 410-km discontinuity: an experimental study. Geophys. Res. Lett. 29. doi:10.1029/2001GL014418.
Stixrude, L., 1997. Structure and sharpness of phase transitions and mantle discontinuities. J. Geophys. Res. 102, 14835–14852.
Stixrude, L., Lithgow-Bertelloni, C., 2005. Thermodynamics of mantle minerals — I physical properties. Geophys. J. Int. 162, 610–632.
Suetsugu, D., Saita, T., Takenaka, H., Niu, F., 2004. Thickness of the mantle transition zone beneath the South Pacific as inferred from analyses of *ScS* reverberated and *Ps* converted waves. Phys. Earth Planet. Int. 146, 35–46.
Tonegawa, T., Hirahara, K., Shibutani, T., 2005. Detailed structure of the upper mantle discontinuities around the Japan subduction zone imaged by receiver function analyses. Earth Planets Space 57, 5–14.
van der Meijde, M., van der Lee, S., Giardini, D., 2005. Seismic discontinuities in the Mediterranean mantle. Phys. Earth Planet. Int. 148, 233–250.
Vinnik, L., 1977. Detection of waves converted from *P* to *SV* in the mantle. Phys. Earth Planet. Int. 15, 39–45.
Vinnik, L., Kosarev, G., Petersen, N., 1996. Mantle transition zone beneath Eurasia. Geophys. Res. Lett. 23, 1485–1488.
Weidner, D., Wang, Y., 1998. Chemical- and Clapeyron-induced buoyancy at the 660 km discontinuity. J. Geophys. Res. 103, 7431–7441.
Weidner, D., Wang, Y., 2000. Phase transformations; implications for mantle structure. In: Karato, S., Forte, A., Liebermann, R., Masters, G., Stixrude, L (Eds.), Earth's Deep Interior: Mineral Physics and Tomography from the Atomic to Global Scale. American Geophysical Union, pp. 215–235.
Zhao, D., 2007. Seismic images under 60 hotspots: search for mantle plumes. Gondwana Res. 12, 335–355.